Shape and motility of a model cell: A computational study

S. V. M. Satyanarayana[a] and A. Baumgaertner
Institut für Festkörperforschung, Forschungszentrum Jülich, 52425 Jülich, Germany

(Received 22 January 2004; accepted 9 June 2004)

We have investigated the shape, size, and motility of a minimal model of an adherent biological cell using the Monte Carlo method. The cell is modeled as a two dimensional ring polymer on the square lattice enclosing continuously polymerizing and depolymerizing actin networks. Our lattice model is an approximate representation of a real cell at a resolution of one actin molecule, 5 nm. The polymerization kinetics for the actin network are controlled by appropriate reaction probabilities which correspond to the correct experimental reaction rates. Using the simulation data we establish various scaling laws relating the size of the model cell to the concentration of polymerized and unpolymerized actin molecules and the length of the enclosing membrane. The computed drift velocities, which characterize the motility of the cell, exhibit a maximum at a certain fraction of polymerized actin which agrees with physiological fractions observed in experiments. The appearance of the maximum is related to the competition between the polymerization-induced protrusion of the membrane and the concomitant suppression of membrane fluctuations. © *2004 American Institute of Physics.* [DOI: 10.1063/1.1778151]

I. INTRODUCTION

The migration of a biological cell plays a prominent role in normal physiological processes as well as in pathology. Examples are embryogenesis, wound healing, and metastasis. Basic to our understanding of the functional aspects of migration are the physical principles of cell motility and chemotaxis. Cell motility and chemotactic migration are related to changes in cell shape which are due to specific rearrangements of the actin cytoskeleton. These rearrangments often involve a rapid response of actin, which polymerizes into new filaments in regions of the cell that are specified by the activated signaling cascades at the plasma membrane following reception of extracellular stimuli.[1–4] These signals give rise to cell polarity and directional motility, by tightly regulating protrusion, adhesion, and cell body translocation processes. In the absence of chemotactic stimuli, cells exhibit persistent random walk.

Theoretical studies of cell motility began with investigations on the mechanism responsible for membrane protrusion. The polymerization of actin filament network is central to protrusion. The earliest models, trying to explain how the polymerization of a rigid polymer (actin filament) can push a load, elaborated the Brownian Rachet mechanism built on thermodynamic ideas.[5] The first implementation of this model[6] considered polymerization of an immobile filament near a fluctuating load. The fluctuations of the load provide enough space for monomers to intercalate at the tip of the growing polymer. As the filament elongates, it prevents (ratchets) the backward motion of the load and thus moves it forward. Modifications of this basic model include the effect of fluctuating elastic filaments.[7] More recently, in the context of movement of microbial pathogen *Listeria* and protein coated beads, this model has been extended to describe the growth and branching of actin filaments at the leading edge of a preexisting array by using either the dentritic nucleation scheme,[8] in which the rate of filament nucleation does not depend on the number of existing filaments, or the autocatalytic branching model,[9,10] in which the filament generation rate explicitly depends on the current filament density. Further, mathematical modeling of actin dynamics at a molecular level as well as at a cell level to understand the protrusion and shape of the leading edge has been achieved.[11,12] However, none of the models proposed so far has considered the effects of a flexible load like a membrane, and neither has taken into account the space-time correlation between the leading and trailing edges of the cellular membrane modulated by the continuously remodeling actin network. Recently, first studies in this direction had been undertaken.[13–15] Here we continue this line of studies focusing on the shape and actin-based motility of a model cell.

In this work we present results of our investigations on the relation between cytoskeletal actin arrangements and the shapes of a cell. Scaling laws between the area of the cell and the amount of polymerized actin network are established. The motility of the cell is characterized by the relation between its drift velocity and the fraction of polymerized actin. The results are based on the analysis of Monte Carlo simulations of a simple model cell. The model and the results are quantitative in the sense that its input parameters such as reaction probabilites and the calculated quantities such as drift velocities can be compared to experimental results.

II. MODEL AND SIMULATION TECHNIQUE

It is not possible presently to model the cell shape and motility in its full generality including all regulatory processes mediated by signaling proteins and valid for all types

[a]Permanent address: Indira Gandhi Centre for Atomic Research, Kalpakkam, India.

of cells. Therefore we restrict our attention to one of the simplest cells, which is the keratocyte residing in the epidermis, the outermost layer of the skin. The keratocyte is involved in the formation of tissue and in wound healing, both requiring the cell's ability to autonomously migrate within the skin tissue. It is in fact one of the fastest moving cells[16] with a speed of 0.5 μm/s. The particular choice of keratocyte is based on the fact that the crescentlike shape of the cell is almost constant as it moves and most of the actin network is stationary relative to substratum, with negligible retrograde flow.[17,18] The motility of the keratocyte is assumed to be based largely on a continuously remodeling actin network. Futhermore, we neglect in our model the cell body, i.e., the nucleus and other organelles. The latter cell type is known as a cytoplast.[19]

A. The geometry and length scales of membrane and actin models

We consider a cell of a keratocyte type or a cytoplast which adheres to a flat substrate in such a way that almost the whole cell is spread out. The adhesion is reversible. In this case and since we are mainly interested in the projected cell shape and the dynamical organization of the cytoskeleton, the cell can approximately be modeled by a flexible ring, representing the cell membrane, which encloses a certain number of actin molecules. For simplicity and computational reasons the cell is modeled on a two dimensional square lattice. The first quantitative input to our model is the size of actin monomer given by 5 nm. We fix the lattice constant of our square lattice to the actin size, $a=5$ nm. We use the Monte Carlo method in order to simulate the model cell. Hence we assume that all particles (membrane, actin molecules) can be described by overdamped Langevin particles.[20]

Membrane. The plasma membrane of a biological cell is a highly complex two-dimensional surface consisting of a lipid bilayer which coexists, among others, with aggregates of integral membrane proteins and a peripheral membrane cortex.[16] Constant remodeling of the cell membrane takes place by various mechanisms as there are, e.g., endocytosis and exocytosis. Since the complexity of the cell membrane cannot be captured by a single model membrane suitable for simulations, we have to restrict our studies to a minimalistic modeling approach and approximate therefore the cell membrane by an elastic two-dimensional ring, similar as in previous successful studies[21] on the thermodynamic behavior of two dimensional vesicles. Specifically, our membrane model is represented by a flexible closed ring embedded on the square lattice. The ring is non-self-avoiding and should exhibit the usual random walk conformation where the enclosed area A and the radius of gyration R scale according to $A\sim R^2\sim L$, where L is the number of segments of the ring on the square lattice. Conformational changes of the ring are achieved by Monte Carlo methods, where randomly chosen pairs of two successive segments of the chain perform a kink jump to one of the neighboring sites. The trial move is rejected if the attempted site is occupied by an actin molecule.

Globular actin (G-actin). The model membrane encloses a fixed number N of actin molecules. Each actin molecule has a size[16] of about 5 nm$\times$5 nm and is located at any of the vertices of the square lattice enclosed by the membrane. The identification of the lattice constant to the size of *G*-actin fixes our length scale. *G*-actin molecules diffuse freely from one lattice point to another. No excluded volume constraint is imposed among *G*-actin molecules. Excluded volume condition, however, is imposed between membrane and *G*-actin molecules, and hence the membrane is impenetrable for actin molecules. The *G*-actin molecules introduce an additional complication. The Brownian motion of the diffusing *G*-actin molecules exerts an internal pressure on the enclosing model membrane, which leads to an expansion of the enclosed area and a strechting of the membrane. The latter effect, although negligible in real cells, has an influence, however, on the shape and motility of our model cell. This is discussed in detail in Sec. II C. It should be noted that in real cells, in contrast to our model cell, the delicate balance between the internal and the external pressure exterted by the cytoplasm and the surrounding media, respectively, is maintained and regulated by a complex signal-mediated network of membrane proteins as channels and transporters and others.[16]

Filament actin (F-actin). The *G*-actin molecules can polymerize and form rigid filaments by association at both ends of an existing filament. The actin monomers in the filaments are called *F*-actin. Excluded volume effect between filaments and diffusing *G*-actin molecule is neglected. Excluded volume effect among filaments, however, is included. The filaments are immobile. This fact takes into account the strong adhesion of *F*-actin to the extracellular substrate mediated by a macromolecular complex containing integrin, vinculin, and other proteins,[22] which are not included explicitly in the cell model. The immobilization of *F*-actin filaments represents the necessary force in order to have a traction of the cell and is necessary to break the symmetry responsible for the conservation of total momentum of the system.

Actin-associated proteins. A host of actin-associated proteins aid the treadmilling of actin network and membrane protrusion. For example, ADF/Cofilin, Profilin, and Thymosine β_4 are involved in sequestration of *G*-actin whereas CapZ and/or Gelsolin cap the growing filaments. Profilin bound ATP–*G*-actin enhances the barbed (fast growing) end association and inhibits the pointed (slow growing) end association. ADF/Cofilin binding to *F*-actin accelerates the pointed end depolymerization. CapZ and Gelsolin cap barbed ends lead to faster growth of uncapped barbed ends. All these actin associated proteins essentially enhance the treadmilling by increasing the asymmetry in the critical concentration of ATP–*G*-actin at barbed and pointed ends. Since our aim is to model the effects of continuously remodeling actin network and fluctuating flexible load like membrane on cell motility, we do not consider the actin associated proteins in our model. A typical snapshot of the simulated cell is depicted in Fig. 1.

B. Probabilities and reaction rates

The Monte Carlo simulation of cell motility involves the implementation of Brownian motion of the membrane and *G*-actin monomers together with the polymerization and depolymerization reactions of actin filaments. Having fixed the

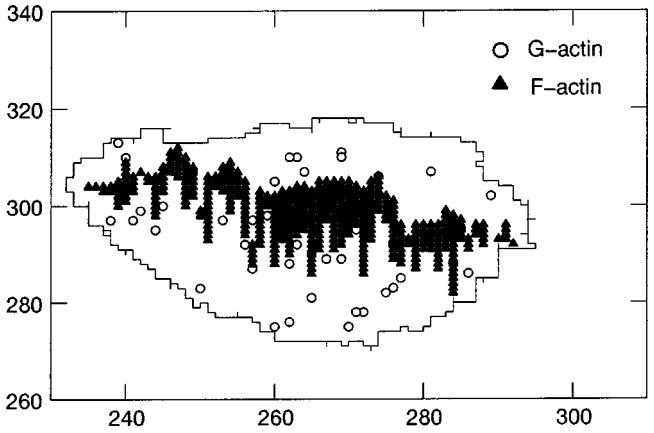

FIG. 1. Snapshot of the model cell. The open circles represent *G*-actin, the filled triangles represent *F*-actin molecules. The length of the membrane is $L=300$, the total number of actin molecules is $N=500$. The length scale is in units of the lattice constant.

lattice spacing to be the size of one *G*-actin monomer, we have then to reconcile the time scale in our simulation with the experimental time scale which can be related to experimental reaction rates. The reaction rate constants in our model simulations, however, cannot be used directly, but have to be implemented in terms of the corresponding reaction probabilities. Therefore, in this subsection, we describe relevant polymerization reactions, the corresponding algorithms, and procedures in order to fix the Monte Carlo time scale and the reaction probabilities.

Polymerization and depolymerization. During the polymerization step the association of a *G*-actin molecule to an existing *F*-actin filament occurs at certain rates at both ends. Since the association of ATP bound *G*-actin can be distinguished between ''barbed'' and ''pointed'' ends, the rate constants k_B^+ and k_P^+, respectively, differ accordingly.[1,16,23,24] The same holds for the depolymerization rates k_B^- and k_P^-, albeit their difference is smaller. The concentration C changes according to the rate equation,

$$\frac{dC}{dt} = -k_{B(P)}^+ C + k_{B(P)}^- . \tag{2.1}$$

Under equilibrium conditions, $dC/dt=0$, and the critical concentrations for barbed and pointed ends are equal, i.e., $C^*=k_B^-/k_B^+=k_P^-/k_P^+$. However, cells under physiological conditions exhibit ATP hydrolysis of Mg-ATP–*G*-actin subsequent to its binding to the barbed end, which leads to an asymmetry in the critical concentrations at the two ends, $k_B^-/k_B^+<k_P^-/k_P^+$. The critical concentrations of ATP–*G*-actin are known from experiments and are approximately 0.1 μM at the barbed end and 0.7 μM at the pointed end.[3] This asymmetry between the critical concentrations at both ends leads to an augmented association of *G*-actin at the barbed end, and an augmented dissociation at the pointed end. This effect is well known and termed ''treadmilling.''[23,24] Indeed, the related gradients of concentration of *G*-actin and their concomitant flow from the rear (trailing edge) to the front (leading edge) of the cell is observed in experiments[25] and in computer simulations.[14]

Nucleation. There are two types of nucleation for *F*-actin. The spontaneous nucleation by forming a binary complex of two *G*-actin molecules with probability W_n, and the ''branching'' nucleation by forming a new filament as a branch from the side of an existing filament. The branching nucleation is modeled following the ''dendritic nucleation'' model.[26–28] It is known that the activated protein complex Arp2/3 (i.e., actin related proteins 2 and 3) can associate with an existing filament and can nucleate there a new filament as a branch from the mother filament at an angle of about 70°. This leads to the formation of a branched network. In our model on the square lattice, the branching process is implemented as follows. If a *G*-actin is found to be on the adjacent row to an existing filament, a new daughter filament is created at this site with probability W_{br}. If there is already a filament in that row, then the nucleation attempt is rejected. The Arp2/3 molecule is not explicitly taken into account in our model because of its large physiological concentration, in particular near the cell membrane where it becomes activated. Therefore it can be assumed that activated Arp2/3 is present at very high concentration within a certain distance r_{ARP} from the cell membrane. However, it can be shown by simulations that the results, as presented in the following section, do not significantly depend on the value of r_{ARP}.

Reaction rules. The reaction and diffusion time scales are different in the present problem and hence after m Monte Carlo cycles, where *G*-actin molecules and the membrane perform random displacements, a reaction cycle starts. One of the actin molecules is randomly selected. Then for either *G*- or *F*-type molecule, a random choice with equal probability is made between an association or dissociation process. The resulting four possible choices lead to the following reactions:

(1) If a dissociation process of *G*-type molecule is chosen, this step is stopped.

(2) If an association process for a *G*-type molecule is chosen, then a successful event may happen, provided one of the ramdomly selected nearest neighbor sites is occupied by either a *G*- or *F*-actin. The *G*-*G* nucleation step takes place with probability W_n. The Arp2/3-mediated branching step, *G*-*F*, takes place with probability W_{br}, provided the selected *F*-actin is located near the membrane within the distance of r_{ARP}. If the selected *F*-actin molecule is one of the ends of a filament, then end polymerization takes place with probability W_B^+ or W_P^+.

(3) If an association process for an *F*-type molecule is chosen, then a successful event may happen, provided one of the ramdomly selected nearest neighbor sites is occupied by a *G*-actin molecule. Analogous to case (2), the Arp2/3-mediated branching step, *G*-*F*, takes place with probability W_{br}, or in case of one of the ends of the filaments, the *G*-*F* end polymerization takes place with W_B^+ or W_P^+.

(4) If a dissociation process for an *F*-type molecule is chosen, then this process takes place with probabilities W_B^- or W_P^-, if the selected *F*-actin molecule is one of the ends of the filaments. Dissociation of a branching point is neglected except for the case where the branching point is the pointed end of a filament.

TABLE I. Experimental values of various parameters used and compared in the present study. The values for $k^{\pm}_{B/P}$ are taken from Ref. 29.

Quantity	Value
Typical cell size	$150\times75\times10$ μm
Lamellipodia size	$10\times5\times0.2$ μm
Actin size	5 nm
Concentration of ATP	200 μM
Concentration of ADP	20 μM
Lamellipod actin concentration	250 μM
Diffusion coefficient of *G*-actin (Ref. 25)	30 $\mu m^2/s$
k_B^+	11.6 $\mu M^{-1}\,s^{-1}$
k_B^-	1.4 s^{-1}
k_P^+	1.3 $\mu M^{-1}\,s^{-1}$
k_P^-	0.8 s^{-1}

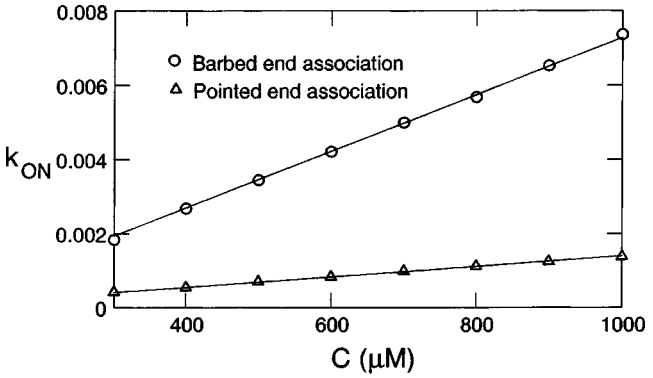

FIG. 2. Number of polymerization events per Monte Carlo step, $k^{\mathrm{ON}}_{B(P)}$, at barbed and pointed ends of a single filament as a function of actin concentration *C*.

Reaction probabilities. Since the experimental reaction rates $k^{\pm}_{B,P}$ cannot be used directly in simulations, but instead reaction probabilities $W^{\pm}_{B,P}$, one has to establish a relation between them. In order to calculate these probabilities, we define $W_B^+=1$ for barbed end polymerization and calculate W_P^+ for the pointed end using the relation

$$\frac{W_P^+}{W_B^+}=\frac{k_P^+}{k_B^+}, \tag{2.2}$$

where the rate constants are the experimental values as listed in Table I. The same can be done for the depolymerization rates $W^-_{B,P}$, which we choose $W_B^-=0.0003$ and calculate W_P^- by using the corresponding relation to Eq. (2.2). The value of W_B^- has been choosen in order to ensure that the filaments are much shorter than the cell size during the simulations.

Monte Carlo step and time scale. A basic question during a simulation combining the Brownian motion of particles and chemical reactions among the particles is their relative time scales. In other words, how many Monte Carlo steps for Brownian motion have to be performed during two sucessive chemical reaction attempts. We have solved that problem by identifying the average reaction time τ as our basic time scale which is then used to estimate the corresponding number of Monte Carlo steps, *m*, from the Brownian motion of the particles. The procedure of calculating *m* is explained in the following subsection.

In principle, the reaction times can be calculated from the ratio of the experimental polymerization rate, $k^+_{B(P)}$, and the rate $\langle k^+_{B(P)}\rangle$ estimated from the simulation of a single filament,

$$t_{B(P)}=\frac{\langle k^+_{B(P)}\rangle}{k^+_{B(P)}}, \tag{2.3}$$

where $\langle k^+_{B(P)}\rangle$ is in units of the number of events per Monte Carlo step and per μM. Therefore we have simulated a single (de)polymerizing filament in a box with periodic boundary conditions containing *N* actin molecules. Just in analogy to *in vitro* experiments, we have performed Monte Carlo simulations of this system with the aim to measure the average rates $\langle k^+_{B(P)}\rangle$ of polymerization. However, $\langle k^+_{B(P)}\rangle$ cannot be measured directly, but rather the number of polymerization events per Monte Carlo step $k^{\mathrm{ON}}_{B(P)}$, which are related to each other by the concentration *C* according to $k^{\mathrm{ON}}_{B(P)}=\langle k^+_{B(P)}\rangle C$. The linear increase of $k^{\mathrm{ON}}_{B(P)}$ with concentration is verified by simulation and shown in Fig. 2. Since the experimental values $k^+_{B(P)}$ are given in units of μM, one has to establish a correspondence between the actin concentration *C* in μM and the number of actin molecules on the square lattice which is calculated as follows. Since 1 mol contains 6.023×10^{23} molecules, 1 μM corresponds[11] to a concentration of 600 molecules per μm^3. Since in our model one lattice site has a volume of 125 nm^3, 1 μM corresponds to 0.75 molecules per 100×100 lattice sites. A typical lamellipod actin concentration in a keratocyte is of the order of 250 μM, which corresponds to 187 molecules per 100×100 lattice sites. We have estimated $\langle k^+_{B(P)}\rangle$ from the slopes of the lines shown in Fig. 2 and have obtained reaction times for polymerization at barbed and pointed ends from Eq. (2.3) using the physiological concentrations and the reaction rates of polymerization at barbed and pointed ends, which are given in Table I. In principle, t_B should be equal to t_P. In our simulation, however, we estimated $t_B=0.658\,\mu$s and $t_P=1.092\,\mu$s. This discrepancy is due to a large statistical error for the small values $k^{\mathrm{ON}}<0.008$. Therefore we fix our simulation time scale as the average of t_B and t_P, $\tau=0.875$ μs. The depolymerization events per Monte Carlo step are also measured. Since depolymerization events are concentration independent, we observe $k^{\mathrm{OFF}}_{B(P)}/W^-_{B(P)}=0.95\pm0.03$, very close to the expected value 1. It should be noted that if one converts the depolymerization events per Monte Carlo step to events per second using the simulation time scale τ, the values $\langle k^-_{B(P)}\rangle$ are two orders of magnitude more than the experimental numbers listed in Table I. This is due to the large depolymerization probability $W_B^-=0.0003$, which we have assumed in order to ensure that the lengths of the filaments do not exceed the size of the simulated model cells. For computational reasons we cannot simulate model cells of many μm diameter comparable to real cells, but rather cells of the order of 1 μm corresponding to $L\leqslant400$. The values of reaction probabilities and the time scale, as used in the Monte Carlo simulations, are summarized in Table II.

TABLE II. Model parameters and reaction probabilities.

Quantity	Value
Lattice constant a	5 nm
Typical cell size	100×100 lattice
Monte Carlo step τ	0.875 μs
W_n	0.01
W_{br}	0.1
W_B^+	1
W_B^-	0.0003
W_P^+	0.11
W_P^-	0.005

C. Brownian motion

Since the polymerization reactions and the Brownian motion of *G*-actins and membrane occur on different time scales, one has to relate the reaction time scale τ to the number of Monte Carlo steps, m, between two successive reaction attempts. One Monte Carlo step is defined, as usual, as one attempted move of all Brownian particles, i.e., *G*-actins and membrane beads.

The diffusion coefficient of a *G*-actin molecule is $D_G = 30\,\mu\mathrm{m}^2/\mathrm{s}$, which is known from experiments.[25] In order to reconcile this value with the value obtained by Monte Carlo simulations of freely diffusing *G*-actins, one has to adjust the number of Monte Carlo steps, m, per time unit τ to their time-dependent mean square displacements $\langle R^2(\tau)\rangle = 4D_G\tau$. Since after a time $\tau=0.875$ μs a *G*-actin has performed a random walk of m steps on the lattice with lattice constant $a=5$ nm, its average mean square displacement is $\langle R^2(\tau)\rangle = a^2 m$, which leads to $m = 4D_G\tau/a^2$, and hence $m \sim 5$.

It should be noted that the present types of reaction-diffusion processes are uncoupled in the sense that a possible diffusion step is performed independent of the following reaction steps. A model of coupled reaction-diffusion processes would require considerations of dependencies of a possible diffusion step on the total local reaction possibilities. The latter model is not considered in the present work. Similarly as in the case of *G*-actin, the number of Monte Carlo steps for the Brownian motion of the membrane beads has to be defined with respect to the time scale τ. One natural choice is the relaxation time T_{mem} of the membrane measured in units of Monte Carlo steps. Simulations of a cell containing unpolymerized *G*-actins provide data for the correlation function of the radius of gyration of the cell membrane, $\langle R^2(t)R^2(0)\rangle$, which decays exponentially according to $\sim\exp(-t/T_{\mathrm{mem}})$. It turned out that the relaxation time is of the same order of magnitude as defined for the *G*-actins, e.g., $m\sim5$ Monte Carlo steps. Therefore, for the sake of simplicity, we also defined for the cell membrane $m=5$ Monte Carlo steps as one unit time step of τ.

In all the following equations and figures, time t is measured in units of $\tau=0.875$ μs and all lengths in units of the lattice constant $a=5$ nm.

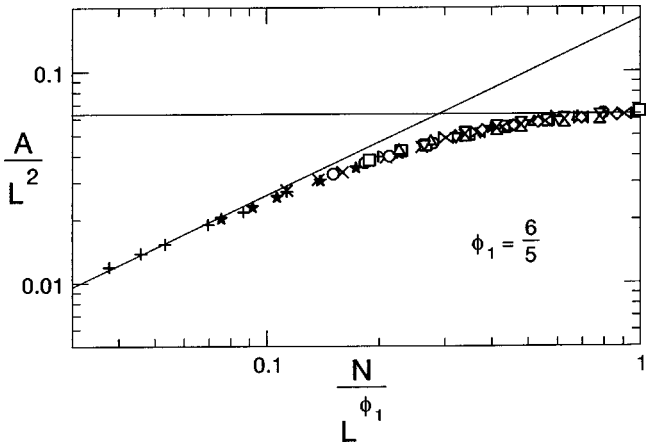

FIG. 3. Scaling of cell area as a function of number of *G*-actins, N, where the symbols correspond to $50\leqslant N\leqslant 500$ in steps of 50, and contour length of membrane, $L=100$, 200, 300, 400, for the case of nonpolymerizing actin.

III. CONFORMATIONS OF A MOTILE CELL

A. Cell containing unpolymerized *G*-actin

In the following paragraph we present the scaling analysis of the cell's area for the case where *G*-actin molecules remain unpolymerized. This is the reference system for the subsequent case of polymerizing actin molecules. The size of the cell depends on the membrane contour length L and the number of *G*-actin monomers, N. The area occupied by the cell exhibits the scaling relation

$$A\sim L^2 f(N/L^{\phi_1}). \tag{3.1}$$

Figure 3 shows the collapse of the data corresponding to the scaling behavior presented in Eq. (3.1). The scaling function has the limiting behaviors

$$f(x)\sim\begin{cases}\text{const} & \text{for } x\gg1\\ x^{1/\phi_1} & \text{for } x\ll1,\end{cases} \tag{3.2}$$

which leads to the asymtotic behaviors for the area of the cell

$$A\sim\begin{cases} L^2 & \text{for } \dfrac{N}{L}\gg1\\[2ex] LN^{1/\phi_1} & \text{for } \dfrac{N}{L}\ll1,\end{cases} \tag{3.3}$$

Using a systematic numerical procedure we have optimized the collapse of the data, as shown in Fig. 3, and found the crossover exponent $\phi_1=1.2\pm0.1$. It is suggestive to assume $\phi_1=6/5$. The asymptotic behavior of scaling function shows that the area is proportional to L^2 in the high-density limit corresponding to an inflated cell, and to L in the low density limit corresponding to random walk ring behavior. In the high-density limit, the monomers diffusing inside exert an internal pressure on the membrane and keep the cell inflated.

In order to compare this result with previous simulations of self-avoiding rings (without internal particles) under a pressure increment between the interior and the exterior,[21] we performed a similar simulation by applying an internal positive pressure on the membrane. The area of the cell

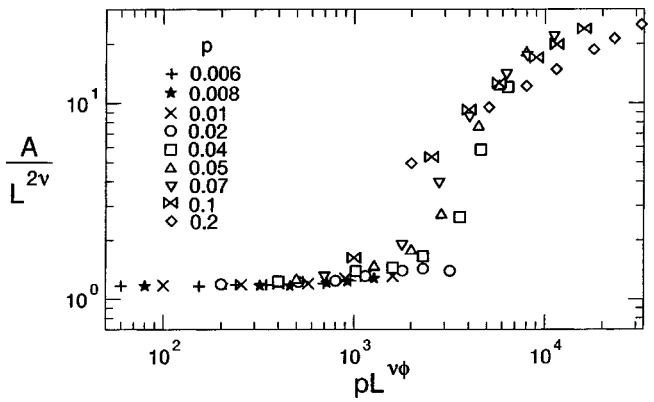

FIG. 4. Scaling of cell area as a function of positive internal pressure.

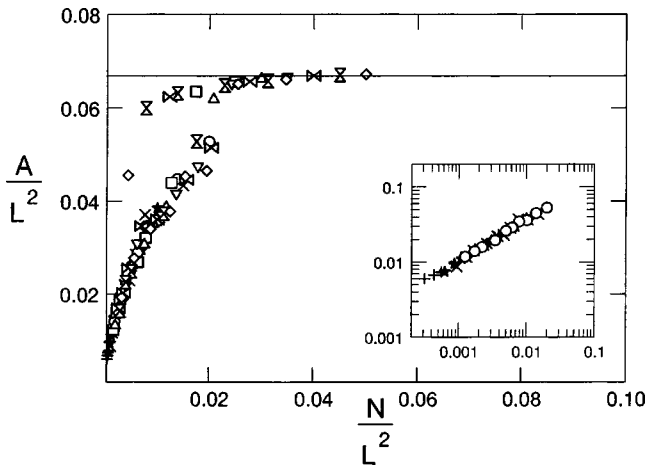

FIG. 5. Scaling of cell area as a function of the number of total actin monomers, N, where the symbols correspond to $50 \leqslant N \leqslant 500$ in steps of 50, and contour length of membrane, $L=100$, 120, 140, 160, 200, 240, 300, 340, 400, for the polymerization case. The inset shows $A \sim L\sqrt{N}$ for small N/L.

obeys the same scaling behavior as observed previously,[21] but with the ideal chain exponent $\nu=1/2$. The scaling behavior

$$A \sim L^{2\nu} f(pL^{\nu\phi}) \tag{3.4}$$

is shown in Fig. 4. The asymptotic behavior of the scaling function is consistent with a Pincus-like argument[21,30]

$$f(x) \sim \begin{cases} x^{2/\phi(1/\nu-1)} & \text{for } x \gg 1 \\ x^{1/\phi(1/\nu-2)} & \text{for } x \ll 1. \end{cases} \tag{3.5}$$

The crossover exponent is fitted to $\phi=2$. This corresponds to the asymptotic behavior of the area

$$A \sim \begin{cases} pL^2 & \text{for } pL \gg 1 \\ L & \text{for } pL \ll 1. \end{cases} \tag{3.6}$$

Comparing the results presented in Figs. 3 and 4, we conclude that the statistical ensemble corresponding to a cell with internal Brownian particles is different and more rich as compared to a cell with an applied positive pressure. However, the asymptotic behaviors of both the scaling functions coincide with respect to their dependence on the length L of the ring.

B. Cell containing polymerizing *F*-actin

We consider in this subsection the case where polymerization and depolymerization are included. In order to examine the shape of a cell, the effect of the *F*-actin filaments is of interest. The result is summarized in Fig. 5 which shows the scaling behavior of the area of a cell containing *G*-actin and polymerized *F*-actin molecules,

$$A \sim L^2 f(N/L^2) \tag{3.7}$$

with the asymptotic bahaviors

$$f(x) \sim \begin{cases} \text{const} & \text{for } x \gg 1 \\ x^{1/2} & \text{for } x \ll 1 \end{cases} \tag{3.8}$$

and hence

$$A \sim \begin{cases} L^2 & \text{for } \dfrac{N}{L} \gg 1 \\ N^{1/2}L & \text{for } \dfrac{N}{L} \ll 1. \end{cases} \tag{3.9}$$

The area of the cell exhibits a discontinuous transition at the critical concentration $c^*=(N/L^2)^* \approx 0.020 \pm 0.003$ from a "motile" phase (Fig. 6), corresponding to a locomoting cell with low *G*-actin concentration, to a "static" phase (Fig. 7), where long *F*-actin filaments are absent and the cell is practically immobile (see also Sec. IV on cell dynamics). The cell assumes an ellipsoidal shape in the motile phase, which compares well with the shapes of keratocytes and cytoplasts.[19] The inflated shape in the static phase is not observed under regular physiological conditions, but we speculate that it may be related to abnormal cell behavior as in cancer where accurate and regulated actin polymerization is absent. The behavior $A \sim L\sqrt{N}$ at low concentrations [Eq. (3.9)] can be understood as follows. At fixed L, the width of the model cell is proportional to L. Since the cell is filled with linear filaments, the length of the cell must be proportional to $\sqrt{N}$ which leads to Eq. (3.9).

The discontinuous transition from the motile to the static phase can also be characterized in terms of the fraction of

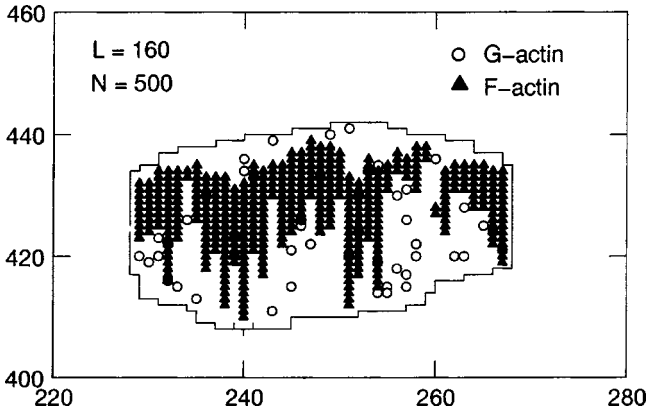

FIG. 6. Snapshot of the model cell at low concentration of *G*-actin in the presence of polymerization processes. Open circles denote *G*-actin, full triangles represent *F*-actin molecules. The length scale is given in units of the lattice constant.

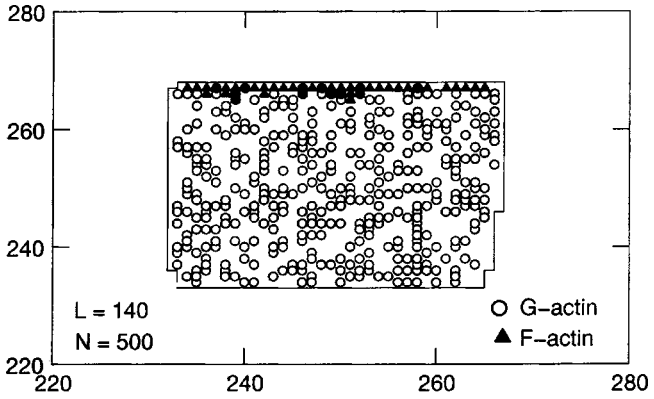

FIG. 7. Snapshot of the model cell at high concentration of *G*-actin in the presence of polymerization processes. Open circles denote *G*-actin, full triangles represent *F*-actin molecules. The length scale is given in units of the lattice constant.

F-actin, N_F/N, as shown in Fig. 8. Consider the case where the length L of the membrane is fixed and the concentration of *G*-actin is continuously increased. For small N, the fraction N_F/N is large, giving rise to movements of the cell. At the critical concentration, $(N/L^2)^*=c^*$, the fraction of *F*-actin discontinuously drops to a low value, which corresponds to the static phase. The fraction of *F*-actin in a motile phase is constant, $N_F/N \approx 0.895 \pm 0.006$, and independent of L and N. This fraction is in agreement with the experimentally measured fraction.[29]

The transition between the motile and the static phases can be understood as follows. Since the fraction N_F/N remains constant at densities $N/L^2 < c^*$, the actual amount of *F*-actin must continuously increase with increasing N/L^2. This leads to a continuous expansion of cell with a concomitant stretching of the cell membrane. Consequently, the fluctuations of the cell membrane become depressed which prohibit further polymerization processes near the leading membrane edge. This allows the depolymerization processes at the rear of the cell to dominate and to shrink the filament network. The cell becomes essentially filled up with *G*-actin only (Fig. 7). The scaling behavior of Eq. (3.9) for low concentrations can also be understood by a simple Flory-type argument. At low concentrations, $c < c^*$, the repulsion between the fluctuating body of continuously polymerizing-

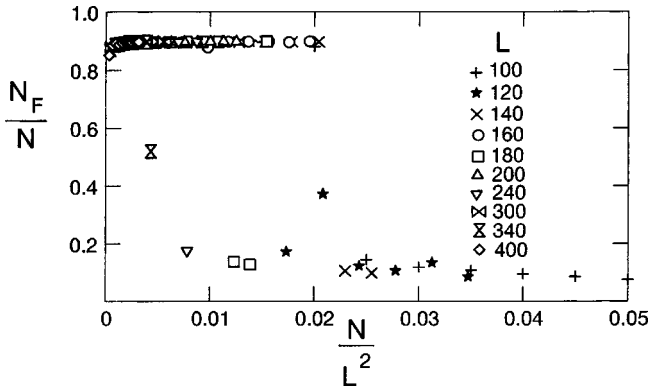

FIG. 8. Scaling of the fraction of *F*-actin, N_F/N, as a function of the actin density N/L^2, $50 \leqslant N \leqslant 500$ in steps of 50.

depolymerizing *F*-actin filaments and the enclosing membrane dominates. Their corresponding concentrations, N/R^2 and L/R^2, respectively, and the radius of gyration of the cell membrane, $R^2 \sim A$, lead to an approximate free energy contribution of repulsion of the order of

$$F_{\text{rep}} \sim \frac{N}{R^d}\frac{L}{R^d}R^d, \tag{3.10}$$

where the space dimension d has been introduced, as usual, for the sake of generality. The entropic contribution to the free energy is attributed to the elastic free energy of the polymer ring by

$$F_{el} \sim \frac{R^2}{L}. \tag{3.11}$$

Minimizing the total free energy $F = F_{\text{rep}} + F_{el}$ with respect to R, one obtains

$$R^2 \sim A \sim N^{2/(d+2)} L^{4/(d+2)}, \tag{3.12}$$

which is in $d=2$ identical to Eq. (3.9). It should be noted that in the case of a self-avoiding polymer ring, $L \equiv N$, the standard Flory result $R \sim L^{3/(d+2)}$ is recovered. These studies show that with respect to the simulations of the cell for motility, the parameters such as membrane contour length L and number of *G*-actin N have to be chosen corresponding to low-density motile phase.

C. Cell with external particles

In real cells a delicate control of the pressure increment between the interior and exterior, i.e., between the cytoplasm and the surrounding media, exists and is maintained and regulated by a complex signal-mediated network of membrane proteins as channels and transporters and others.[16] Experimentally, the pressure increment, $\Delta p \equiv p_{\text{int}} - p_{\text{ext}}$, can be easily controled by, e.g., variation of the osmotic strength of the solvent. In the present model cell, however, we have considered so far (Secs. III A and III B the special situation where the external pressure is $p_{\text{ext}}=0$ and the efflux of particles is strictly prohibited. In principle, the osmotic effect could be taken into account in simulations studies by a chemical potential controling the exchange of molecules between the interior and exterior. This, however, is out of the scope of the present work. But we will consider in the following a special case in order to get a first idea of how the results, as obtained in Secs. III A and III B, do change by considering the effects of external particles on the cell membrane.

We consider the case where the external particle density is the same as that of internal particles. The external particles are also non-self-avoiding and interact with the membrane by excluded volume interaction. We used periodic boundary conditions for the external particles. A typical snapshot of the cell in the environment of external particles and the periodic box is shown in Fig. 9. We simulated both the cases corresponding to a cell without polymerization (Fig. 10) and with polymerization (Fig. 11). The scaling corresponding to the cell with no polymerization is given by

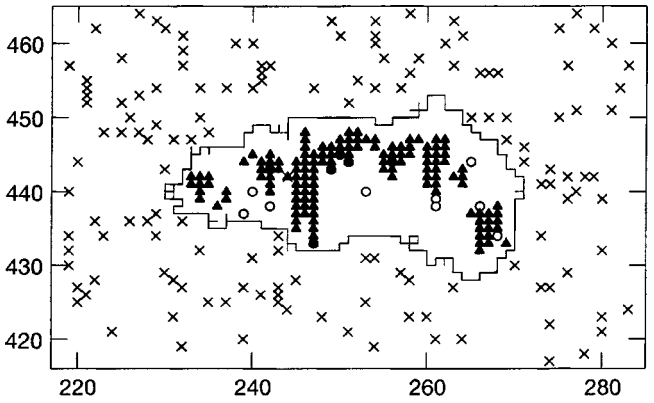

FIG. 9. Snapshot of the cell with particles inside and outside with polymerization.

$$A \sim L^2 f(N/L^{\phi_2}). \tag{3.13}$$

The scaling function has the limiting behaviors

$$f(x) \sim \begin{cases} \text{const} & \text{for } x \gg 1 \\ x^{1/\phi_2} & \text{for } x \ll 1, \end{cases} \tag{3.14}$$

which leads to the asymtotic behavior

$$A \sim \begin{cases} L^2 & \text{for } \dfrac{N}{L} \gg 1 \\ LN^{1/\phi_2} & \text{for } \dfrac{N}{L} \ll 1, \end{cases} \tag{3.15}$$

The crossover exponent is fitted to $\phi_2 = 3/2$. In the low-density limit, the area scales as L as in the case of no external particles. However, the area grows as $N^{5/6}$ in the case of no external particles, whereas it grows as $N^{2/3}$ with external particles. The presence of external particles compensates the pressure exerted by the internal particles and therefore leads to a slower growth of area with increasing N. The simulations of the cell with polymerization in the presence of external particles also show a similar scaling behavior, but with a different crossover exponent. The scaling is given by

$$A \sim L^2 f(N/L^{\phi_3}). \tag{3.16}$$

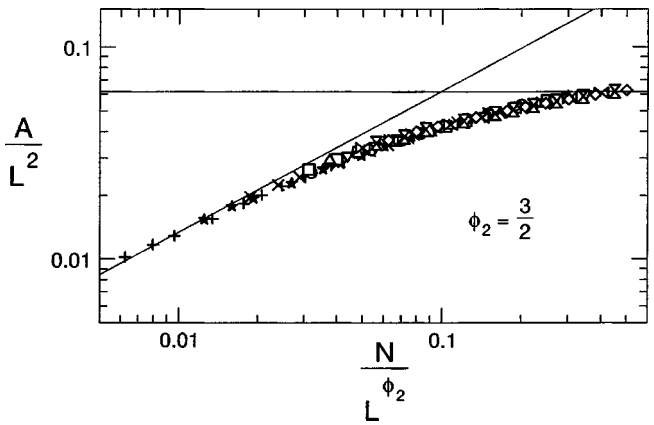

FIG. 10. Scaling of cell area as a function of number of G-actins, N, where the symbols correspond to $50 \leqslant N \leqslant 500$ in steps of 50, and contour length of membrane, $L = 100,120,...,400$, for the nonpolymerization case and in the presence of external particles.

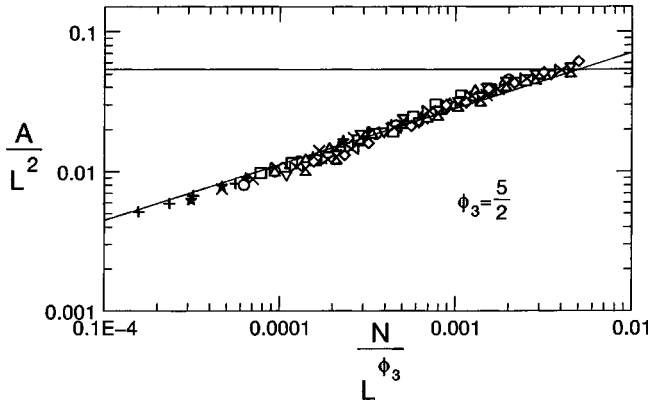

FIG. 11. Scaling of cell area as a function of number of G-actins, N, where the symbols correspond to $50 \leqslant N \leqslant 500$ in steps of 50, and contour length of membrane, L, for the polymerization case and in the presence of external particles.

The crossover exponent is fitted to $\phi_3 = 5/2$ and the asymptotic behavior is given by

$$A \sim \begin{cases} L^2 & \text{for } \dfrac{N}{L} \gg 1 \\ LN^{1/\phi_3} & \text{for } \dfrac{N}{L} \ll 1. \end{cases} \tag{3.17}$$

Analogous to the no-polymerization case, we observe a slower growth of area with increasing N in the presence of external particles. As can be seen from Fig. 11, the discontinuous transition observed in Fig. 5 is absent and the area shows a smooth transition towards the inflated limit.

IV. CELL DYNAMICS

The polarization of the cell is fundamental to the directed migration of the cell. The cell polarity is macroscopically characterized by the formation of leading and trailing membrane edges which is a consequence of the asymmetric distributions of the growing and shrinking ends of the actin cytoskeleton. This spontaneous internal polarity determines the direction of cell motion and is maintained without external signals (e.g., chemotaxis) for a certain time (persistent random walk). The complex signal transduction pathways with positive and negative feedback loops regulate the formation of cell polarity, but we do not discuss the details which are beyond the scope of this paper. We note that different signals converge on the activation of an Arp2/3 protein complex, which leads to branching and autocatalytic polymerization.

A. Persistent random walk

It was shown theoretically and by simulations[13] that the Arp2/3-induced branching process corresponds to an autocatalytic polymerization[31] which gives rise to a persistent random walk of the cell as observed in experiments.[1,2,32] During this type of motion the cell moves with almost constant velocity in one direction for a certain time until it spontaneously changes its direction of motion. The trajectory of the center of our model cell is shown in Fig. 12 as a typical example from our simulations. Persistent random walk can

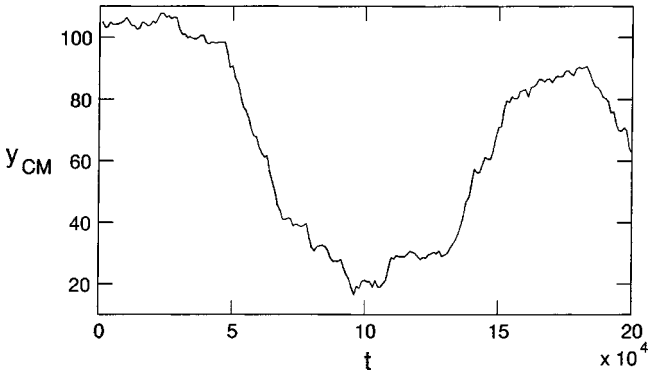

FIG. 12. The trajectory of a cell exhibiting persistent random walk.

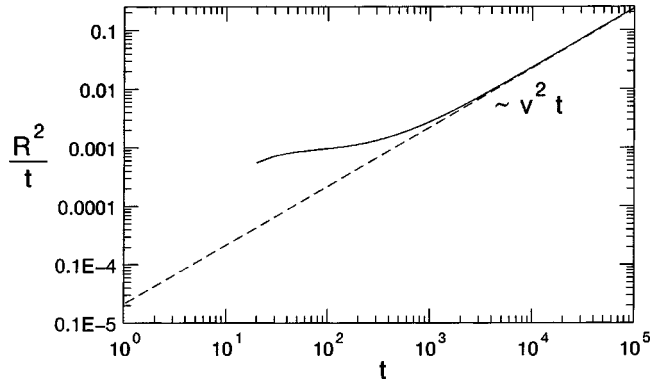

FIG. 14. Typical mean square displacement of the center of a cell exhibiting directed motility, $N=200$, $L=200$.

be obtained by using the present model, where the simulations are carried out with small monomer concentration, high treadmilling rate, and Arp2/3-induced branching near the cell membrane at both sides of the cell with respect to the Y direction. During a nucleation process, where two G-actin monomers form a F-actin filament, the subsequent growth direction of the linear filament is chosen at random. Since it is experimentally known that Arp2/3 is activated close to the membrane, we perfom branching from an existing filament only if the filament extends to a certain neighborhood of the membrane. In our simulations we choose the width of this range to be 0.2 times the size of the cell. As expected, the cell exhibits a persistent random walk which can also be decuced from the time-dependent mean square displacement (Fig. 13). The dynamics at short and long times are governed by diffusion, whereas for intermediate times, the cell motion exhibits a drift. The spontaneous change of the direction of motion can be qualitatively understood as follows. If the branching initiates in one direction, there will be an explosive growth of filaments in that direction due to the autocatalytic nature of polymerization kinetics and hence the cell moves in that direction. When the filament network is sufficiently dense, then it suppresses the membrane fluctuations allowing the depolymerization to dominate and free up the monomers. This facilitates the filaments in the opposite side to grow and change the direction of the cell.

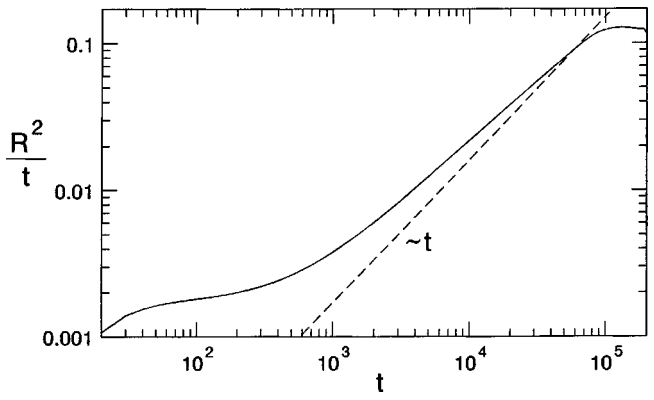

FIG. 13. Typical mean square displacement of a cell exhibiting a persistent random walk.

B. Drift velocity

The motility of a cell can be characterized by its drift velocity. As discussed above, the cell persists to move in one direction before it changes its direction. In prinicple, the drift velocity can be estimated from the persistent random walk. However, for the sake of convenience and clarity in computing the drift velocity we consider here the case of a unidirectional motility only. This can be achieved by confining the Arp2/3-induced branching to only one direction. We study the drift velocity as a function of the fraction of F-actin, N_F/N. Since the fraction of F-actin is controled by the reaction probabilities $W_{B/P}^{\pm}$, we choose to vary the pointed end depolymerization probability, W_P^-. The variation of W_P^- is directly related to the tuning of the treadmilling process, which in turn is related to the average filament length and to the network remodeling time. Increasing W_P^- results in shortening the filament length and in a faster remodeling of the network. Further, W_P^- also controls the monomer pool, which is important for barbed end polymerization.

A typical example of the time-dependent mean square displacement per time, $\langle R^2(t)\rangle/t$, of the center of the cell versus time is shown in Fig. 14. At short times the cell exhibits diffusion and at long times a unidirectional drift. The drift velocity is estimated by fitting the data in the drift regime to a straight line with a unit slope.

Figure 15 shows the drift velocity as a function of W_P^-. It is observed that the drift velocity exhibits a maximum at $W_P^- = W^* \approx 0.013$ which is independent of N. Moreover, the drift velocity is independent of N for the whole range $W_P^- < W^*$ and follows approximately a power law $v \sim (W_p^-)^{0.91\pm0.02}$. For $W_P^- > W^*$, the drift velocity falls off exponentially and more rapidly for large N. This can be qualitatively understood as follows. The locomotion of the cell is governed by the treadmilling of the actin network. Arp2/3 induced branching creates more barbed ends than pointed ends and enhances the polymerization at the leading edge. This, in turn, requires an adequate monomer reservoir in order to maintain the steady state treadmilling process. At $W_P^- < W^*$, due to branching and autocatalytic polymerization, a filament network is formed with a high fraction of F-actin and a small fraction of G-actin. If W_P^- becomes larger, the G-actin population increases. This leads to an in-

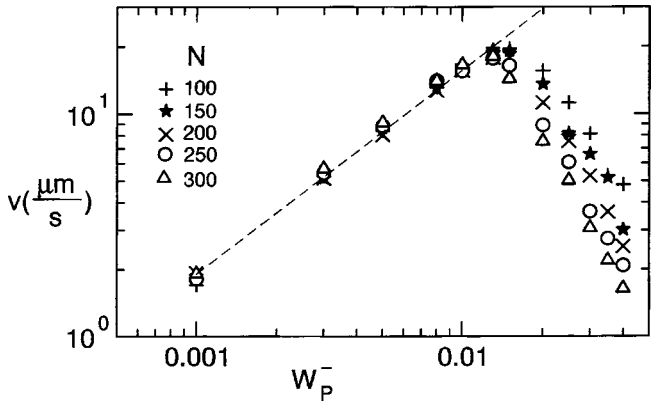

FIG. 15. Log-log plot of scaled drift velocity as a function of pointed-end depolymerization probablity W_p^- for various N, $L=200$. The broken line is a fit indicating a power law $\sim(W_p^-)^{0.91}$ for small W_p^-.

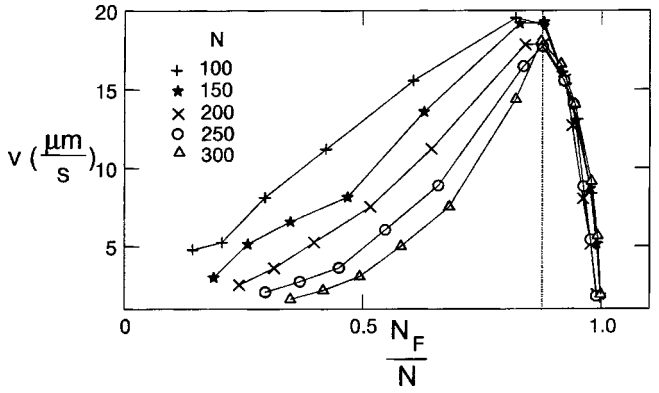

FIG. 17. Drift velocity as a function of the fraction of F-actin N_F/N for various N, $L=200$. The vertical line corresponds to the optimal fraction that maximizes the velocity.

creased number of polymerization events at the barbed ends, and consequently the velocity becomes larger. In the range of $W_P^- < W^*$ the treadmilling of an actin network occurs almost in the form of a single cluster. With increasing W_P^- the average filament length decreases and the velocity reaches an optimum value at W^*. For $W_P^- > W^*$, the network breaks into smaller clusters, which are short living and inefficient in pushing the membrane and hence the velocity decreases rapidly. Thus, the region $W_P^- < W^*$ is characterized by the presence of large long living treadmilling actin networks, while at $W_P^- > W^*$ short living small clusters of actin filament networks exist.

The existence of large actin networks and their decomposition into smaller cluster can be deduced from the fraction of F-actin, N_F/N, which is shown in Fig. 16 for one cell size L. At $W_P^- \ll W^*$ the fraction is close to its saturation. With increasing W_P^- the fraction N_F/N decreases slowly, almost independent of the total number of actin N and approximately according to a power law $N_F/N \sim (W_P^-)^{-0.044\pm0.003}$. In the range $W_P^- > W^*$, the fraction of F-actin decreases rapidly depending strongly on N, which indicates the decomposition of large networks into smaller clusters.

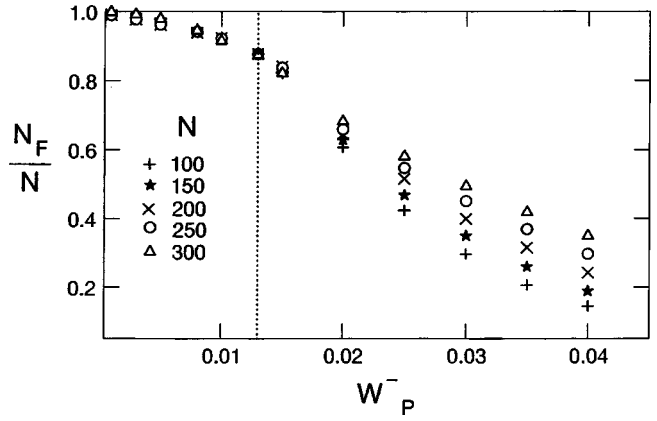

FIG. 16. Fraction of F-actin, N_F/N, as a function of pointed-end depolymerization probablity W_p^- for various N, $L=200$. The dotted line indicates the maximum of the velocity at $W_p^- = W^*$.

The dependency of the drift velocity on the amount of F-actin is shown in Fig. 17. The velocity exhibits a maximum for an optimal value of the fraction of F-actin, $(N_F/N)^* \approx 0.877 \pm 0.002$, which is in agreement with physiological fractions known from experiments,[29] other theoretical estimates,[11] and our own estimate in the preceding section for a motile phase (Fig. 8). It is observed that for $N_F/N > (N_F/N)^*$ the velocity decreases rapidly and almost independent of N, whereas for $N_F/N < (N_F/N)^*$ the velocity decreases more gradually and depends strongly on the concentration of actin, N/L^2, at fixed $L=200$.

Below the threshold $(N_F/N)^*$, the dependency of v on N, i.e., the rapid decrease of the velocity with increasing N at a given value of N_F/N, can be understood based on two competing mechanisms. Increasing N at fixed N_F/N means that the number of membrane pushing barbed ends per membrane length increases which would lead to an increase of the velocity. This promoting effect, however, is diminished by the concomitant increase of suppression of the membrane fluctuations which reduces the cell's velocity. The appearance of the maximum of v as a function of N_F/N at fixed N is based on the same competitive effect: an increasing amount of barbed ends enhances the events of polymerization, but suppresses at the same time the frequency of membrane fluctuations. The first effect dominates at $N_F/N < (N_F/N)^*$, whereas the second effect prevails above the threshold.

Our data seem to indicate that the maximal velocity at the threshold is independent of N and of the order of $v \sim 18\,\mu$m/s. This value, however, is one order of magnitude higher as compared to experimentally measured keratocyte speeds. An explanation for this discrepancy can be attributed to the approximate and minimal representation of our model cell as compared to real keratocytes. The model is two dimensional, and the nucleus and a host of cytoplasmic constituents, responsible for possible retarding effects, are not included.

It is interesting to note that the simulation results of Fig. 17 can be compared to analytical considerations by Mogilner and Edelstein-Keshet.[11] Their data, as depicted in Fig. 6 of

their paper,[11] show a qualitatively similar behavior as our data in Fig. 17: a maximal velocity at a certain density of leading barbed ends. However, the physical origin of the maximum in their approach is somewhat different from ours. In their case, the optimal velocity is due to a competition between the number of barbed ends and the number of available *G*-actins: the more barbed ends, the larger the velocity which holds until the maximum where too many barbed ends start to deplete the monomer pool significantly and hence the number of membrane-pushing polymerization events decrease drastically. In our case, however, the decrease in the velocity with increasing density of barbed ends is due the concomitant barbed-end-induced suppression in membrane fluctuations. It is conceivable that the latter effect is not an artifact of our simple cell model, but rather a significant feature in cell motility.

V. CONCLUDING REMARKS

Despite the fact that the present cell model contains some very simple minimal representations of certain features of a keratocyte or a cytoplast, the corresponding results from Monte Carlo simulations can be compared to experiments and other analytical approaches. In particular, the fraction of *F*-actin corresponding to the maximum velocity agrees well with the physiological fractions measured in experiments. Since the physical reason for the appearance of the critical values, $v_{\max}$ and $(N_F/N)^*$, which is based on the competition between the frequencies of barbed end polymerization and membrane fluctuations, became evident from our simulations, further studies are required on more elaborate cell models, e.g., in three dimensions, and using more realistic membrane models, in order to corroborate the present observations and physical interpretations.

ACKNOWLEDGMENT

S.V.M.S. would like to thank the Institut für Festkörperforschung at the Forschungzentrum Jülich for providing a postdoctoral fellowship.

[1] D. Bray, *Cell Movements*, 2nd ed. (Garland, New York, 2001).
[2] D. A. Lauffenburger and A. F. Horwitz, Cell **84**, 359 (1996).
[3] T. D. Pollard and G. G. Borisy, Cell **112**, 453 (2003).
[4] M.-F. Carlier, C. L. Clainche, S. Wiesner, and D. Pantaloni, BioEssays **25**, 336 (2003).
[5] T. L. Hill and M. W. Kirschner, Int. Rev. Cytol. **78**, 1 (1982).
[6] C. Peskin, G. Odell, and G. Oster, Biophys. J. **65**, 316 (1993).
[7] A. Mogilner and G. Oster, Biophys. J. **71**, 3030 (1996).
[8] A. Mogilner and G. Oster, Biophys. J. **84**, 1591 (2003).
[9] A. E. Carlsson, Biophys. J. **81**, 1907 (2001).
[10] A. E. Carlsson, Biophys. J. **84**, 2907 (2003).
[11] A. Mogilner and L. Edelstein-Keshet, Biophys. J. **83**, 1237 (2002).
[12] H. Grimm, A. Verkhovsky, A. Mogilner, and J.-J. Meister, Eur. Biophys. J. **32**, 563 (2003).
[13] R. Sambeth and A. Baumgaertner, Phys. Rev. Lett. **86**, 5196 (2001).
[14] R. Sambeth and A. Baumgaertner, Journal of Biological Systems **9**, 201 (2001).
[15] A. Baumgaertner and R. Sambeth, J. Chem. Phys. **111**, 5223 (1999).
[16] B. Alberts, D. Bray, A. Johnson, J. Lewis, M. Raff, K. Roberts, and P. Walter, *Essential Cell Biology* (Garland, New York, 1998).
[17] J. Theriot and T. Mitchison, Nature (London) **352**, 126 (1991).
[18] J. Lee, A. Ishihara, J. Theriot, and K. Jacobson, Nature (London) **362**, 167 (1993).
[19] A. B. Verkhovsky, T. M. Svitkina, and G. G. Borisy, Curr. Biol. **9**, 11 (1999).
[20] K. Kikuchi, M. Yoshida, T. Maekawa, and H. Watanabe, Chem. Phys. Lett. **185**, 335 (1991).
[21] S. Leibler, R. P. Singh, and M. E. Fisher, Phys. Rev. Lett. **59**, 1989 (1989).
[22] K. A. DeMali and K. Burridge, J. Cell. Sci. **116**, 2389 (2003).
[23] A. Wegner, J. Mol. Biol. **108**, 139 (1976).
[24] Y. L. Wang, J. Cell Biol. **101**, 597 (1985).
[25] V. C. Abraham, V. Krishnamurthy, D. L. Taylor, and F. Lanni, Biophys. J. **77**, 1721 (1999).
[26] T. M. Svitkina and G. G. Borisy, J. Cell Biol. **145**, 1009 (1999).
[27] K. J. Amann and T. D. Pollard, Nat. Cell Biol. **3**, 306 (2001).
[28] T. D. Pollard and C. C. Beltzner, Curr. Opin. Struct. Biol. **12**, 768 (2002).
[29] T. Pollard, L. Blanchoin, and R. Mullins, Annu. Rev. Biophys. Biomol. Struct. **29**, 545 (2000).
[30] P. Pincus, Macromolecules **9**, 386 (1976).
[31] D. Pantaloni, R. Boujemaa, D. Didry, P. Gounon, and M.-F. Carlier, Nat. Cell Biol. **2**, 385 (2000).
[32] D. Shreiber, V. Barocas, and R. Tranquillo, Biophys. J. **84**, 4102 (2003).